Optics Letters

Multimodal imaging system combining optical coherence tomography and Brillouin microscopy for neural tube imaging

Yogeshwari S. Ambekar,[1] Manmohan Singh,[1] Alexander W. Schill,[1] Jitao Zhang,[2] Christian Zevallos-Delgado,[1] Behzad Khajavi,[1] Salavat R. Aglyamov,[3] Richard H. Finnell,[4] Giuliano Scarcelli,[5] and Kirill V. Larin[1,6,*]

[1]Department of Biomedical Engineering, University of Houston, Houston, Texas, USA
[2]Department of Biomedical Engineering, Wayne State University, Detroit, Michigan, USA
[3]Department of Mechanical Engineering, University of Houston, Houston, Texas, USA
[4]Departments of Molecular and Cell Biology, Molecular and Human Genetics, and Medicine, Baylor College of Medicine, Houston, Texas, USA
[5]Fischell Department of Bioengineering, University of Maryland, College Park, Maryland, USA
[6]Department of Molecular Physiology and Biophysics, Baylor College of Medicine, Houston, Texas, USA
*Corresponding author: klarin@uh.edu

Received 21 January 2022; revised 3 February 2022; accepted 3 February 2022; posted 4 February 2022; published 3 March 2022

To understand the dynamics of tissue stiffness during neural tube formation and closure in a murine model, we have developed a multimodal, coaligned imaging system combining optical coherence tomography (OCT) and Brillouin microscopy. Brillouin microscopy can map the longitudinal modulus of tissue but cannot provide structural images. Thus, it is limited for imaging dynamic processes such as neural tube formation and closure. To overcome this limitation, we have combined Brillouin microscopy and OCT in one coaligned instrument. OCT provided depth-resolved structural imaging with a micrometer-scale spatial resolution to guide stiffness mapping by Brillouin modality. 2D structural and Brillouin frequency shift maps were acquired of mouse embryos at gestational day (GD) 8.5, 9.5, and 10.5 with the multimodal system. The results demonstrate the capability of the system to obtain structural and stiffness information simultaneously.

https://doi.org/10.1364/OL.453996

Congenital anomalies can lead to lifelong disabilities which significantly impact not only the individual but society at large. Neural tube defects (NTDs) are the second most common form of congenital structural birth defects. Neural tube formation and closure comprise tightly-orchestrated complex processes that are crucial for proper embryogenesis. When the transient developmental structure of the neural tube fails to close during neurulation, it results in structural and functional abnormalities of the developed central nervous system. The bending, shaping, and fusion of the neural plate, and the propagation of neural tube closure (NTC) along the length of the body axis, are all biomechanical events [1]. Moreover, biomechanical influences may signal cells, alter critical gene expression patterns, and modify cell shape, cell kinetics, and cell survival [2]. Hence, these mechanical influences, such as tissue stiffness, can lead to NTDs because they are critical to NTC [3]. The fact that extrinsic forces can prevent proper NTC [4] strongly suggests that a precise balance between forces and neural plate tissue stiffness is required to achieve neural fold fusion under normal developmental conditions. Currently, the nature of the cellular motors required for the initiation, progression, and completion of NTC is poorly understood. Among all the tightly coordinated morphogenetic events involved in NTC, perhaps the most critical is the actual migration of the neural folds towards one another [4–6]. When the neural folds elevate and approach each other, there must be a transient release of physical contact between the neural ectoderm and the surface ectoderm, which is then restored with their corresponding tissue layer on the opposite neural fold to secure the closure of the neural tube [7].

Understanding of the dynamic interplay between forces and tissue stiffness during NTC is required for novel intervention strategies as well as for developing new treatment paradigms *in utero* and following the birth of infants with such congenital defects. Hence, both structural and mechanical imaging of neural tube formation and closure is required to fully understand NTC. Techniques for mechanical imaging to understand tissue stiffness, like atomic force microscopy [8], acoustic radiation force elastography [9], and micro-indentation with optical coherence elastography (OCE) [10], have been used to determine the elasticity of developing embryos. However, these techniques have low resolution and are contact-based or invasive, which may affect the developing embryos. Brillouin microscopy is a noninvasive optical imaging technique capable of mapping the longitudinal modulus of tissue with high spatial resolution without contact [11–13]. However, Brillouin microscopy is relatively slow to map large areas and cannot provide structural information, limiting its applicability for dynamic processes such as neurulation. Imaging structural information is crucial for understanding the physical location of tissue stiffness. Optical coherence tomography (OCT) is a well-established technique

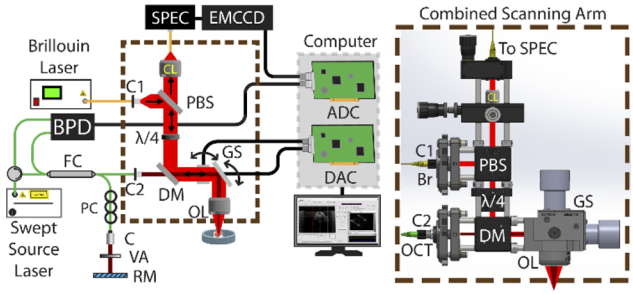

Fig. 1. Schematic of integrated OCT + Brillouin system. ADC: analog to digital convertor, BPD: balanced photodetector, Br: Brillouin, C, C1, C2: collimator, CL: collection lens, DAC: digital to analog converter, DM: dichroic mirror, FC: fiber coupler, GS: galvo scanning mirrors, λ/4: quarter-wave plate, PBS: polarizing beam splitter, OL: objective lens, PC: polarization controller, RM: reference mirror, VA: variable attenuator, SPEC: dual-stage virtual image phase array spectrometer, EMCCD: electron multiplying charged coupled device camera.

that can noninvasively provide 3D structural details of developing embryos with high resolution [14,15]. While biomechanical information can be gleaned with the elastographic extension of OCT, i.e. OCE [16], it almost always requires active tissue stimulation, which can be detrimental to delicate embryo tissues. We have previously established the synergy between OCT and Brillouin microscopy to image embryonic neural tubes, but we used separate systems and sequential imaging, which is not feasible for live imaging [17,18]. Here, we adapted, optimized, and combined the two technologies to build a single OCT-Brillouin instrument for structurally-guided tissue stiffness mapping of the neurulation process.

Figure 1 is a schematic of the developed coaligned multimodal Brillouin microscopy and OCT imaging system. The imaging sub-systems were combined with a custom scanning arm, which is shown in the dashed boxes in Fig. 1. The OCT system consisted of a swept source laser (HSL-20, Santec USA, Corp., Hackensack, New Jersey) with a central wavelength of ~1310 nm, scan range of ~105 nm, and a scan rate of 50 kHz. The OCT incident power on the sample was ~8 mW, and the OCT system sensitivity was 103 dB. OCT imaging time during 2D and 3D acquisition was 20 ms and 22 s, respectively.

The Brillouin light source was a single-mode 660 nm laser (Torus, Laser Quantum Inc., Fremont, CA), which provided an optimized Brillouin signal considering the absorption from the sample as well as the intrinsic efficiency of Brillouin scattering [19]. The galvo mirrors accommodated a maximum 4 mm beam diameter, so the Brillouin light was collimated to a $1/e^2$ diameter of 3.37 mm (C1 in Fig. 1, TC18FC-633, Thorlabs Inc., NJ, USA) to the input of the combined scanning arm. This was in turn combined with the OCT probe beam via a dichroic mirror. A polarizing beam splitter (PBS) and a quarter-wave plate (QWP) was used to minimize the losses. The vertically-polarized laser light was reflected off the PBS to reach the sample, and all scattered light was transmitted through the PBS to reach the spectrometer. Brillouin microscopy is a confocal modality and thus a high numerical aperture (NA) objective lens results in high-resolution images. However, this also severely restricts the depth of focus for OCT. We tested different objective lenses capable of acquiring OCT and Brillouin data simultaneously and in this study used an achromatic doublet (AC080-010-B-ML, Thorlabs. Inc) with an NA of 0.25 for the Brillouin system, resulting in a lateral resolution of 3.8 μm and an axial resolution of 36 μm, which was measured using a beam profiler (LaserCam-HR II 2/3-inch, Coherent Inc., Santa Clara, CA). The axial and OCT transverse resolutions in air were ~9.8 μm and ~17.5 μm, respectively. The working distance of the achromatic doublet was 7 mm, and the transverse field of view was 2 × 2 mm, with the chromatic focal shift corrected in the acquisition software. The Brillouin light incident on the sample was ~35 mW. The theoretical and calculated insertion losses in the sample arm for the Brillouin microscopy system were ~3 dB and for the OCT system were ~6 dB.

The backscattered Brillouin light collected by the achromatic doublet was coupled into a single-mode fiber by an aspheric lens (CL in Fig. 1; C397TMD-A, Thorlabs Inc.) with a 0.3 NA and delivered to a high-resolution Brillouin spectrometer. The Brillouin microscopy system consisted of a two-stage virtually imaged phased array (VIPA) spectrometer [20]. Within the spectrometer, light collimated from the single-mode fiber was focused on the input window of the first VIPA, which angularly separated the different spectral components of the backscattered light. After the first VIPA, a cylindrical lens transformed the angular separation into a spatial separation at its focal plane. Unwanted spectral components were then rejected through a slit acting as a spatial filter. A set of lenses imaged the plane of the slit onto the second VIPA entrance window to reduce crosstalk. After the second VIPA, the light was filtered by a second spatial filter and subsequently focused onto an electron-multiplying charge coupled device (EMCCD) camera (iXon Andor, Belfast, UK). The Brillouin frequency shift was determined based on the spectrum recorded by the EMCCD camera. The exposure time of the camera was 0.2 s. The frequency precision of the system was measured as 6.5 MHz for water and acetone and 10.0 MHz in gelatin phantoms of various elasticities, which correspond to the longitudinal modulus precision of ~0.3%. Before any measurements, the system was calibrated using standard materials, including water, acetone, and methanol.

Traditionally, the sample is translated during Brillouin imaging for 2D or 3D imaging, but this would drastically slow down OCT imaging. Hence, a pair of galvanometer-mounted mirrors were used in the combined scanning head. In the combined system, both the OCT beam and Brillouin beam were scanned using the galvo scanners. However, the sample must still be translated along the optical axis for Brillouin imaging, so a motorized vertical stage was integrated into the system. For large-scale lateral translation of the sample, two additional stages were incorporated. To control both imaging systems, the motorized stages, and acquire Brillouin and OCT images simultaneously, we developed custom imaging control software in the LabVIEW environment (NI, TX, USA). The alignment of the OCT and Brillouin beams was first checked with a beam profiler. Then, the co-registration was calibrated with a water–glass–water phantom. The software was capable of simultaneous Brillouin and OCT imaging and precise translation of the sample in three dimensions. The user can rapidly acquire structural images of the samples with OCT and select regions of interest for Brillouin imaging.

In this study, we set up timed matings of CD-1 mice overnight. The mice were checked for the presence of a vaginal plug every morning, and the morning a plug was found was considered as gestation day (GD) 0.5. Neural tube formation starts at GD 8,

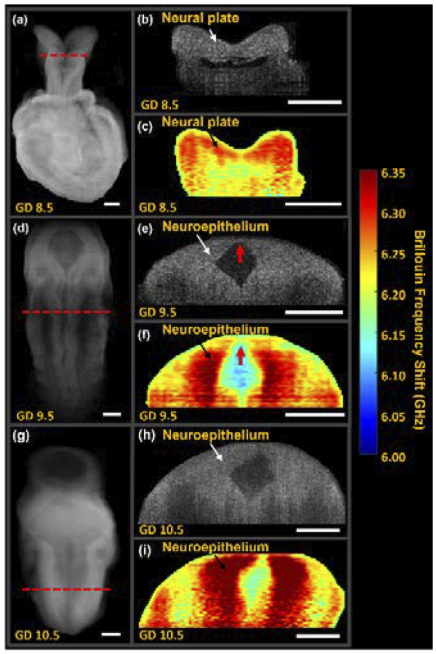

Fig. 2. (a), (d), (g) 3D-OCT images of GD 8.5, 9.5, and 10.5, respectively. (b), (e), (h) 2D-OCT images of mouse embryo neural tube at (a)–(c) GD 8.5 (open), (d)–(f) 9.5 (closed) and (g)–(i) 10.5 (closed). (c), (f), (i) 2D Brillouin images of mouse embryos at corresponding Brillouin frequency shift maps. (Scale bars are 0.2 mm).

and the neural tube closes completely by the end of GD 9.5 [14], so we performed the OCT + Brillouin imaging at GD 8.5, 9.5, and 10.5. The mice at the respective gestation days were euthanized with CO_2 inhalation followed by cervical dislocation. The embryos were dissected with temperature maintained at 37°C and then kept in culture media [21] in an incubator (37°C and 5% CO_2). The yolk sac was removed during dissection to access the neural tube region of the embryos. The embryos were left to recover for one hour in the incubator immediately after dissection. They were then transferred to 1.5% agarose gel (A4718, Sigma-Aldrich Inc., Saint Louis, MO) plates where they were oriented such that the neural tube faced up. The agarose plates were then carefully filled with culture media. All the OCT + Brillouin measurements were taken on the fresh embryos within six hours of dissection. All the procedures were performed under approved protocols of the University of Houston and Baylor College of Medicine Institutional Animal Care and Use Committees. Three dimensional OCT images were initially acquired to locate the desired neural tube area. Then the desired region of interest for Brillouin imaging was selected from the 2D OCT image using the instrument software. The Brillouin images were acquired with a step size of 10 µm and 100 × 100 pixels, and the total imaging time was ~33 minutes.

Figure 2 shows the 3D OCT images (1000 A-lines, 1000 B-scans), 2D OCT images, and 2D Brillouin shift maps of mouse embryos at (a-c) GD 8.5, (d-f) GD 9.5, and (g-i) GD 10.5. From the Brillouin shift images at GD 8.5, the cell-dense layer of the neural plate has a much greater Brillouin shift than the surrounding tissues, indicating that the neural plate is stiffer. At GD 9.5, the neural plate forms the neuroepithelial layer, which is also cell-dense as shown by the greater Brillouin frequency shift compared to the surrounding tissue. Similarly, at GD 10.5,

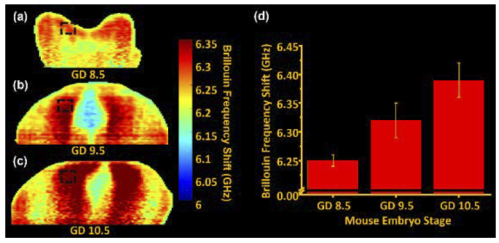

Fig. 3. (a)–(c) 2D Brillouin images of mouse embryos at GD 8.5, 9.5, and 10.5, respectively. (d) Average Brillouin frequency shift of neuroepithelium (dashed box) for corresponding embryo stage.

the neuroepithelium layer was stiffer than the mesoderm and the ectoderm layer. Figure 3 shows quantifications of the neural plate and subsequent neuroepithelium. The part of the neural plate region denoted by the dotted box in Fig. 3(a) had a mean Brillouin frequency shift of 6.25 ± 0.01 GHz. As noted earlier, the neural plate then forms into the neuroepithelium during neurulation. The average Brillouin frequency shift of neuroepithelium region for GD 9.5 and 10.5 shown by the dotted boxes in Figs. 3(b) and (c) were 6.32 ± 0.03 GHz and 6.39 ± 0.03 GHz, respectively. During the development, the stiffness of the neuroepithelium layer increased, which is shown by the Brillouin frequency shift of the region plotted in Fig. 3(d). Moreover, the neural tube appears to be closed in the OCT structural image in Fig. 2(e), but the Brillouin image in Fig. 2(f) shows that the neural tube, particularly the neuroepithelium, is not actually completely fused (shown by red arrows), which corroborates our previous work [18] and demonstrates the usefulness of the mechanical contrast for neurulation imaging.

The Brillouin frequency shift can be converted into the longitudinal modulus (M) given that the tissue mass density (ρ) and refractive index (n) is known [22]. The values of ρ and n can vary within the tissue but the ratio ρ/n^2 is relatively constant for many biological tissues [11,23], so the majority of changes in Brillouin frequency shift are due to variation in the longitudinal modulus.

In this study, we demonstrated that the coaligned OCT + Brillouin system could simultaneously map structural and biomechanical properties completely noninvasively. The multimodal system could map the distribution of the longitudinal modulus of the neural tube in mouse embryos with OCT guidance at various developmental stages. The biomechanical properties of mouse embryos at GD 8.5 are different to those at GD 9.5 and GD 10.5, as seen by the increase in Brillouin frequency shift of the neural plate and neuroepithelium tissues, which coincides with an increase in cellular density [24]. Brillouin imaging adds additional contrast through mechanical mapping, which can provide complementary information to structural imaging.

The quantitative link between the Brillouin frequency shift and elastic modulus is not established in biological tissue. Brillouin microscopy probes the longitudinal modulus at high (GHz) frequencies and micron-scale resolution, which contrasts with the macroscopic measurements of Young's modulus at physiological timescales [11]. However, many experiments in the past decade have established strong empirical correlations between Brillouin-probed mechanical properties and traditional stress-strain techniques in many biological tissues [13,25,26]. These correlations are believed to result from the common dependence of longitudinal and Young's moduli on underlying biophysical

factors and characteristics of biological samples. For example, in this case, neuroepithelial cells are more densely packed than other cells in the embryonic neural tube during development [27]. Cellular density is also a determinant of tissue stiffness, which drives higher longitudinal modulus [28]. Although the link between the Brillouin-measured stiffness can be confounded by other parameters, such as hydration [22], modern Brillouin instruments are sensitive enough to recognise the differences in tissues [25] because hydration is relatively similar in many tissues and cells. The NA is relatively low in the current system compared to most other Brillouin microscopy systems, which reduces the axial and lateral resolution. This can be seen in the transition regions between the tissue and surrounding media, such as around the periphery of the neural plate and neural folds in Fig. 2(c). Another reason for this blurring could be the dependence of Brillouin spatial resolution on acoustic phonon propagation length. However, the use of a higher NA objective lens would limit the depth of focus of the OCT system, although this could potentially be ameliorated by, e.g., Gabor-domain style OCT imaging [29]. Moreover, the spatial resolution of Brillouin measurement is affected by both optical parameters and material properties, such as the phonon wavelength and propagation length [30]. Therefore, additional work is needed to determine the optimal NA for the combined Brillouin + OCT system. Other elastography techniques, such as OCE, which is a functional extension of OCT, can be used in conjunction with Brillouin microscopy, but OCE lacks the spatial resolution of Brillouin microscopy. To achieve the resolution of the Brillouin technique, OCE excitation has to be in the order of 100 MHz [31]. Another limitation of the system is the use of relatively widely-separated wavelengths. The use of the dichroic mirror did not produce any artifacts but it did introduce additional losses. Moreover, the objective lens antireflection coating was optimized for Brillouin. Thus, there were reflection artifacts in the OCT images, which were minimized by imaging at a depth beyond the artifacts. The incident power on the sample was safe for Brillouin imaging as we observed no physical damage to the embryos in the OCT images or visually after Brillouin imaging. Recent work has shown that even greater power levels with higher NA lenses showed no damaged cells [19].

Our future work is focused on further optimizations of the multimodal imaging system. Currently, the OCT and Brillouin measurements are acquired in sequence due to the acquisition time of Brillouin imaging. However, in the future, we plan to integrate the use of multiple objectives, e.g., low NA lens first to acquire OCT and automatically change to a high NA lens to acquire the Brillouin image. In addition, we will be evaluating the biomechanical properties of NTDs in murine models and performing live imaging, which is the main benefit of the coaligned imaging system.

Funding. National Science Foundation (DBI-1942003); National Institutes of Health (P30EY07551, R01HD095520, R01EY030063, K25HD097288).

Disclosures. RHF formerly held a leadership position in the now-defunct consulting company TeratOmic Consulting LLC. He also receives travel funds to attend editorial board meetings of the Reproductive and Developmental Medicine journal.

Data availability. Data underlying the results presented in this paper are not publicly available at this time but may be obtained from the authors upon reasonable request.

REFERENCES

1. E. Nikolopoulou, G. L. Galea, A. Rolo, N. D. Greene, and A. J. Copp, Development **144**, 552 (2017).
2. D. E. Ingber, FASEB J. **20**, 811 (2006).
3. Y. Yamaguchi and M. Miura, Cell. Mol. Life Sci. **70**, 3171 (2013).
4. R. Massarwa and L. Niswander, Development **140**, 226 (2013).
5. I. S. Alvarez and G. C. Schoenwolf, J. Exp. Zool. **261**, 340 (1992).
6. T. Nishimura and M. Takeichi, Development **135**, 1493 (2008).
7. H. J. Ray and L. Niswander, Development **139**, 1701 (2012).
8. N. R. Chevalier, E. Gazguez, S. Dufour, and V. Fleury, Methods **94**, 120 (2016).
9. J. Park, J. Lee, S. T. Lau, C. Lee, Y. Huang, C. L. Lien, and K. Kirk Shung, Ann. Biomed. Eng. **40**, 907 (2012).
10. M. Marrese, N. Antonovaite, B. K. A. Nelemans, T. H. Smit, and D. Iannuzzi, Acta Biomater. **97**, 524 (2019).
11. G. Scarcelli, W. J. Polacheck, H. T. Nia, K. Patel, A. J. Grodzinsky, R. D. Kamm, and S. H. Yun, Nat. Methods **12**, 1132 (2015).
12. G. Scarcelli and S. H. Yun, Nat. Photonics **2**, 39 (2008).
13. Y. S. Ambekar, M. Singh, J. Zhang, A. Nair, S. R. Aglyamov, G. Scarcelli, and K. V. Larin, Biomed. Opt. Express **11**, 2041 (2020).
14. S. Wang, M. D. Garcia, A. L. Lopez 3rd, P. A. Overbeek, K. V. Larin, and I. V. Larina, Biomed. Opt. Express **8**, 407 (2017).
15. S. Wang, I. V. Larina, and K. V. Larin, Biomed. Opt. Express **11**, 2017 (2020).
16. K. V. Larin and D. D. Sampson, Biomed. Opt. Express **8**, 1172 (2017).
17. R. Raghunathan, J. Zhang, C. Wu, J. Rippy, M. Singh, K. V. Larin, and G. Scarcelli, J. Biomed. Opt. **22**, 1 (2017).
18. J. Zhang, R. Raghunathan, J. Rippy, C. Wu, R. H. Finnell, K. V. Larin, and G. Scarcelli, Birth Defects Res. **111**, 991 (2019).
19. M. Nikolić and G. Scarcelli, Biomed. Opt. Express **10**, 1567 (2019).
20. K. V. Berghaus, S. H. Yun, and G. Scarcelli, J. Vis. Exp. **106**, e53468 (2015).
21. V. K. Kalaskar and J. D. Lauderdale, J. Vis. Exp. **85**, 50803 (2014).
22. P. J. Wu, I. V. Kabakova, J. W. Ruberti, J. M. Sherwood, I. E. Dunlop, C. Paterson, P. Torok, and D. R. Overby, Nat. Methods **15**, 561 (2018).
23. G. Scarcelli, R. Pineda, and S. H. Yun, Invest. Ophthalmol. Visual Sci. **53**, 185 (2012).
24. S. G. McShane, M. A. Mole, D. Savery, N. D. Greene, P. P. Tam, and A. J. Copp, Dev. Biol. **404**, 113 (2015).
25. G. Scarcelli and S. H. Yun, Nat. Methods **15**, 562 (2018).
26. G. Scarcelli, P. Kim, and S. H. Yun, Biophys. J. **101**, 1539 (2011).
27. E. Graham, J. Moss, N. Burton, C. Armit, L. Richardson, and R. Baldock, Development **142**, 1909 (2015).
28. I. P. Weber, S. H. Yun, G. Scarcelli, and K. Franze, Phys. Biol. **14**, 065006 (2017).
29. C. Canavesi and J. P. Rolland, Appl. Sci. **9**, 2565 (2019).
30. G. Antonacci, T. Beck, A. Bilenca, J. Czarske, K. Elsayad, J. Guck, K. Kim, B. Krug, F. Palombo, R. Prevedel, and G. Scarcelli, Biophys. Rev. **12**, 615 (2020).
31. M. A. Kirby, K. Zhou, J. J. Pitre, L. Gao, D. Li, I. Pelivanov, S. Song, C. Li, Z. Huang, T. Shen, R. Wang, and M. O'Donnell, J. Biomed. Opt. **24**, 1 (2019).